

# Rotating Disks and Non-Kinematic Double Peaks

Moshe Elitzur<sup>1</sup>, Andrés Asensio Ramos<sup>2</sup> and Cecilia Ceccarelli<sup>3</sup>

<sup>1</sup>*Department of Physics & Astronomy, University of Kentucky, Lexington, KY 40506, USA; moshe@pa.uky.edu*

<sup>2</sup>*Instituto de Astrofísica de Canarias, 38205, La Laguna, Tenerife, Spain; aasensio@iac.es*

<sup>3</sup>*Laboratoire d'Astrophysique de l'Observatoire de Grenoble, BP 53, 38041 Grenoble, Cedex 9, France; Cecilia.Ceccarelli@obs.ujf-grenoble.fr*

Accepted 2012 February 7. Received 2012 January 13; in original form 2011 December 6

## ABSTRACT

Double-peaked line profiles are commonly considered a hallmark of rotating disks, with the distance between the peaks a measure of the rotation velocity. However, double-peaks can arise also from radiative transfer effects in optically thick non-rotating sources. Utilizing exact solutions of the line transfer problem we present a detailed study of line emission from geometrically thin Keplerian disks. We derive the conditions for emergence of kinematic double peaks in optically thin and thick disks, and find that it is generally impossible to disentangle the effects of kinematics and line opacity in observed double-peaked profiles. Unless supplemented by additional information, a double-peaked profile alone is not a reliable indicator of a rotating disk. In certain circumstances, triple and quadruple profiles might be better indicators of rotation in optically thick disks.

**Key words:** radiative transfer — line: formation — line: profiles — methods: numerical — ISM: lines and bands — galaxies: active — quasars: emission lines

## 1 INTRODUCTION

Rotating disks are key elements in numerous astrophysical systems. Protoplanetary disks around young stellar objects (YSOs) are where planets eventually form, and thus are of paramount importance in all theories of planet formation. Mass transfer in cataclysmic variables (CVs) proceeds through an accretion disk around the white dwarf. In active galactic nuclei (AGNs), the accretion disks are the conduit of material to the central black hole and the source of continuum emission at all wavelengths shorter than IR. Unfortunately, small angular sizes preclude direct imaging of the disks in most CVs and YSOs, and virtually all AGNs; only a handful of AGNs provide direct evidence for Keplerian disks through interferometric observations of water masers (see Greenhill 2007). In the absence of imaging, a double-peaked line profile is often taken as evidence for an inclined rotating disk, with the distance between the peaks a measure of the rotation velocity. For example, the detection of double-peaked profiles has been used to establish the presence of disks in AGNs (see Eracleous et al. 2009, and references therein), and the analysis of double-peaked profiles has been used to deduce the mass of the central object from the derived Keplerian rotation (Zhang et al. (2008)).

In the widespread reliance on the double-peaked profile as a marker of rotating disks it has been overlooked that such a profile may actually result not from disk rotation but, instead, from purely radiative transfer effects in optically thick, non-rotating systems. As has long been known, the simplest line transfer problem involving a uniform, quiescent slab without any large-scale motions leads to double-peaked profiles at large optical depths (see Avrett & Hummer 1965, and references therein). Unfortunately, the existence of

these *non-kinematic double peaks* has been largely overlooked. Instead, the Horne & Marsh (1986) seminal work introduced flat-top line profiles for the optically thick segments of rotating disks, an approximation that ignores the spatial variation of the source function. A number of recent detailed calculations of line emission from protoplanetary systems did produce double-peaked profiles in some optically thick face-on disks (Pavlyuchenkov et al. 2007; Cernicharo et al. 2009; Ceccarelli et al. 2010), but the implications of these results were not discussed. The significance of non-kinematic double peaks has been noted only relatively recently by Hummel (2000) in the context of B[e] stars.

Our goal here is to present a general study of line emission from rotating disks to determine whether and when the effects of kinematics and line opacity can be disentangled in observed double-peaked profiles. Following Horne & Marsh we consider a geometrically-thin Keplerian disk and compute its line emission profile for a large range of optical depths with detailed radiative transfer calculations. The radiative transfer problem for a non-rotating geometrically thin uniform disk is identical to that for an infinite uniform slab when neglecting radiation propagation in the plane. In §2 we demonstrate the emergence of non-kinematic double peak profiles, without any large scale motions, in the line emission from optically thick uniform slabs; in Appendix A we derive some simple analytic expressions that approximate adequately the exact calculations. In §3 we present the solution for Keplerian disks, which shows double peak line emission from face-on viewing. We study the properties of kinematic double peaks, which are introduced by the disk rotation, and compare them with the non-kinematic ones. Section §4 contains a discussion.

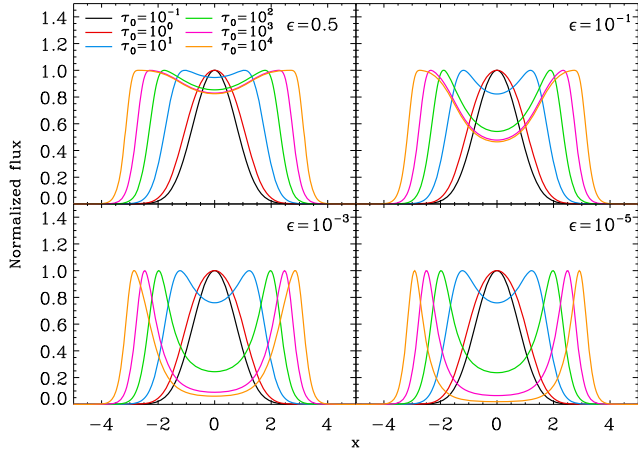


**Figure 1.** Frequency profiles  $\Psi(x)$  of line radiation from a uniform slab, normalized to a unity peak flux, from exact numerical calculations with the CEP method. Each panel corresponds to a different value of the photon destruction probability  $\epsilon$  (see eq. 1). Different lines correspond to different values of  $\tau_T$ , the line-center slab optical depth, as marked.

## 2 NON-KINEMATIC DOUBLE PEAKS

To demonstrate the formation of double-peaked profiles in the absence of any large scale motions we start with the simplest problem involving the smallest possible number of free parameters—a uniform slab with constant temperature and density and no radiation other than line radiation generated internally by collisions. We solve the problem with the Coupled Escape Probability (CEP); this is an exact method we developed recently for the line transfer problem that offers great speed advantages over traditional computational approaches (Elitzur & Asensio Ramos 2006). We consider line emission from a transition between upper level  $u$  and lower level  $l$  separated by energy  $E_{ul} = h\nu_0$ . The transition properties are fully specified for line transfer calculations by the parameter  $\epsilon$ , the photon destruction probability defined through

$$\frac{\epsilon}{1 - \epsilon} = \frac{C_{ul}}{A_{ul}} (1 - e^{-E_{ul}/kT}) \equiv \frac{n}{n_{\text{crit}}} \quad (1)$$

Here  $C_{ul}$  and  $A_{ul}$  are, respectively, the collisional de-excitation rate and the spontaneous emission coefficient,  $T$  is the gas temperature,  $n$  the density and  $n_{\text{crit}}$  the transition critical density corrected with the Boltzmann factor (see, e.g., eq. 24 in Elitzur & Asensio Ramos 2006). Vertical position in the slab can be specified by the coordinate  $\tau$ , the optical depth at line center which varies from 0 to  $\tau_T$  between the two faces. Denote by  $\Delta\nu_D$  the frequency width of the thermal motions then the optical depth at every frequency is

$$\tau(x) = \tau\Phi(x), \quad \text{where} \quad x = \frac{\nu - \nu_0}{\Delta\nu_D} \quad (2)$$

and where  $\Phi(x)$  is a profile normalized to unity at line center. The problem is fully specified by just two free parameters,  $\epsilon$  and  $\tau_T$ , and the line absorption profile. In the numerical calculations here we take  $\Phi$  as Gaussian,  $\exp(-x^2)$ , but the results are applicable to other profiles, for example Lorentzian shape.

Figure 1 shows the frequency profiles  $\Psi(x)$  of the line radiation leaving the slab vertically for different sets of the free parameters  $\epsilon$  and  $\tau_T$ . In optically thin slabs,  $\Psi(x) = \Phi(x)$ . Double-peaked profiles emerge when  $\tau_T \geq 10$  and become more pronounced as  $\epsilon$  gets smaller, i.e., as the density decreases away from the critical density. As noted in the Introduction, double-peaked profiles in optically thick sources are a well known radiative transfer effect

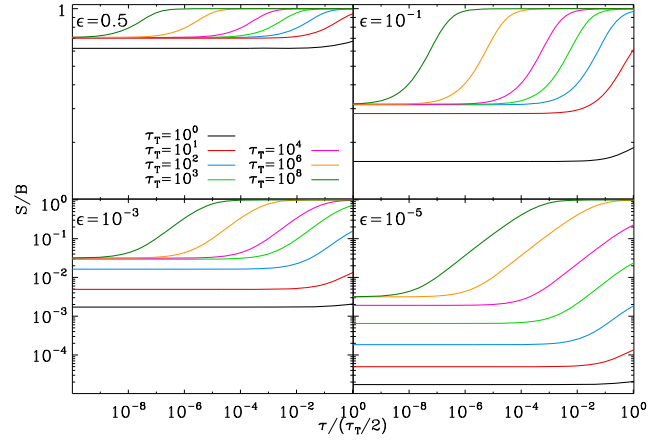


**Figure 2.** Variation of the source function, normalized by the Planck function of the slab temperature, with optical depth into the slab for the models shown in figure 1. The profiles are symmetric about the slab midplane, which is the endpoint of the horizontal axis in each panel. Because the axis is scaled with the overall optical depth, the same point in each panel indicates a different distance from the surface. Note also that  $S/B = 1$  implies a thermalized transition ( $T_x = T$ ).

(e.g., Avrett & Hummer 1965). The explanation is rather simple. Consider a slab whose line center optical depth to the midplane exceeds unity. Then the frequency  $x_c$  where  $\frac{1}{2}\tau_T\Phi(x_c) = 1$  defines the line core, the spectral region  $|x| < x_c$  in which each half of the slab is optically thick. Similarly, the frequency  $x_w$  where  $\tau_T\Phi(x_w) = 1$  defines the line wings—the entire slab is optically thin at  $|x| > x_w$ . For the Doppler profile, the explicit expressions for these two frequencies are

$$x_w = \sqrt{\ln \tau_T}, \quad x_c^2 = x_w^2 - \ln 2 \quad (3)$$

At the line core,  $|x| < x_c$ , each half of the slab is optically thick and the radiation emerges from an optical distance of only  $\sim 1$  from each surface. Thus the line core intensity is roughly the value of the source function  $S$  at position  $\tau = e^{x^2}$  (see eq. A3); that is, the core spectral shape reflects the spatial variation of  $S$ , or, equivalently, the line excitation temperature  $T_x$  since  $S = B(T_x)$  where  $B$  is the Planck function (e.g., Elitzur 1992). Because of photon trapping,  $T_x$  is maximal on the slab midplane, declining toward each surface. So the core intensity decreases from a peak at  $|x| = x_c$ , corresponding to the magnitude of  $T_x$  on the midplane, to a minimum at line center, where it reflects the excitation temperature at distance  $\tau = 1$  from the surface. At the line wings,  $|x| > x_w$ , the slab is optically thin everywhere and its emission is simply  $I(x) = \bar{S}\tau_T\Phi(x)$ , where  $\bar{S}$  is the value of the source function at some intermediate point inside the slab (see appendix A); that is, the spectral shape of emission at the wings follows the line profile,  $\Psi(x) = \Phi(x)$ . The intensity now decreases as  $x$  increases because the entire slab is fully visible and the optical depth decreases away from line center.

Figure 2 shows the spatial profile of  $S/B$ , where  $B(T)$  is the Planck function of the (constant) slab temperature, vs optical depth into the slab for a large range of  $\epsilon$  and  $\tau_T$ . This spatial variation is directly reflected in the properties of the emerging radiation profile (fig. 1). Once the level populations reach thermal equilibrium,  $T_x = T$  and  $S/B = 1$ . When  $\tau_T \gg 1/\epsilon$ , the transition is thermalized at slab center as is evident from the figure (see also eq. A6). Approaching the slab surface, photon escape reduces  $T_x$  and the source function is decreasing, producing the intensity dip at line center. When  $\tau_T$  increases, thermalization spreads from the slab midplane

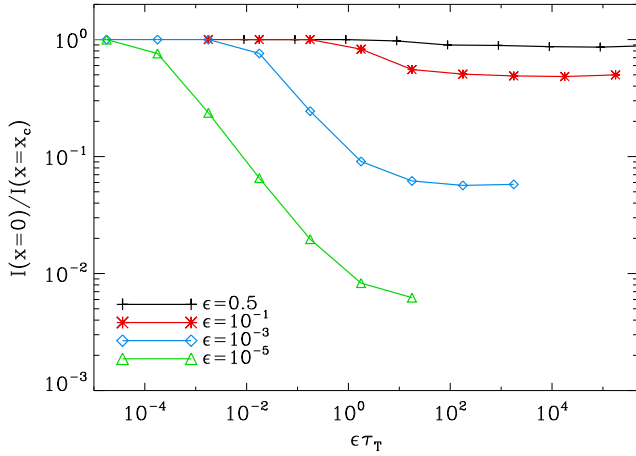


**Figure 3.** Variation of the depth of the line profile central dip with slab optical thickness for various values of  $\epsilon$ ; the horizontal axis reflects the problem's scaling properties. When  $\tau_T \gg 1/\epsilon$ , the depth of the dip saturates at a value that varies roughly as  $\sqrt{\epsilon}$  (see eq. 4).

toward its surfaces, larger portions of the source have  $T_x \simeq T$  and the peaks flatten out. This flattening becomes more pronounced as  $\epsilon$  increases, i.e.,  $n$  approaches  $n_{\text{crit}}$ . When  $\tau_T < 1/\epsilon$ , the level populations do not reach thermal equilibrium even at slab center, but photon trapping ensures that  $T_x$ , and the source function, is always higher there than at the surface.

The behavior of the central dip seen in fig. 1 is readily explained by the spatial variation of the source function. The depth of the dip can be characterized by the ratio of intensities at line center and at the peaks. Figure 3 shows the variation of this ratio with optical thickness for various values of  $\epsilon$ ; because of the scaling properties of the problem (see eq. A6), the horizontal axis is labeled with  $\epsilon\tau_T$ . For every  $\epsilon$ , the dip reaches maximal depth when  $\tau_T \gg 1/\epsilon$ . The dip essentially disappears at  $\epsilon = 0.5$ , corresponding to  $n = n_{\text{crit}}$ , because the source function thermalizes throughout most of the slab; in this regime,  $S(\tau)$  is nearly flat across the line core (see fig. 2). In Appendix A we discuss these issues further and derive semi-analytic approximations that describe adequately the exact numerical results; in particular, fig. A1 reproduces the line profiles quite accurately with simple analytic expressions. The depth of the central dip is accurately described by eq. A7; to a good degree of approximation, its large- $\tau_T$  limit is

$$\frac{I_{\min}}{I_{\max}} = \frac{I(x=0)}{I(x=x_c)} \simeq \frac{1}{\epsilon\tau_T} \simeq \sqrt{\epsilon} \quad (4)$$

(see eq. A8). This approximation describes reasonably well the results shown in figure 3.

This standard problem demonstrates that double-peaked profiles need not require any large scale motion because they are generated naturally by radiative transfer effects. We will refer to these as *non-kinematic double peaks*. In very optically thick sources, the emergent radiation peaks at the frequency shifts  $x \simeq \pm x_c$ , producing a peak separation of

$$\Delta v_{\text{peak}} \simeq 2x_c \Delta v_D \simeq 2\Delta v_D \sqrt{\ln \tau_T} \quad (5)$$

Outside the peaks, the intensity falloff traces the shape of the Doppler wings. Inside the peaks, the intensity falloff toward line center reflects the spatial decline of the source function, i.e., the line excitation temperature, when the surface is approached.

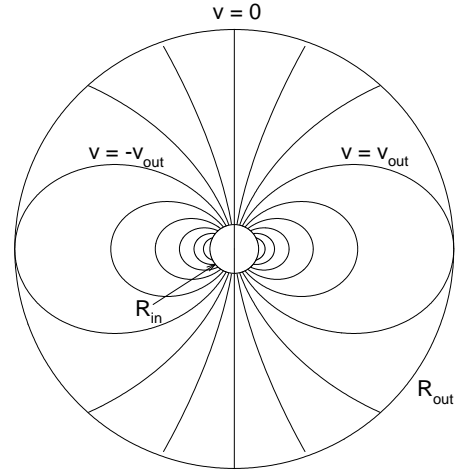


**Figure 4.** Contours of constant line-of-sight (los) velocity  $v$  for a Keplerian disk between radii  $R_{\text{in}}$  and  $R_{\text{out}}$ . The observer is along the  $v = 0$  contour. In the 1st quadrant, the los velocity increases along successive contours clockwise from the top.

### 3 ROTATING DISK LINE PROFILES

#### 3.1 Basic Theory

Consider a geometrically-thin disk, extending from an inner radius  $R_{\text{in}}$  to  $R_{\text{out}} = YR_{\text{in}}$ . The intensity toward angle  $i$  from the disk normal is  $I_v(R, i)$ , where  $R$  is axial radius. Then the flux observed at distance  $D$  and viewing angle  $i$  ( $< 90^\circ$ ) is  $L_v(i) \propto (\cos i/D^2)$ , where

$$L_v(i) = \int I_v(R, i) dA \quad (6)$$

is the disk monochromatic luminosity in direction  $i$ . The observed flux is obtained from an integration over the circular surface area even though the disk image is an ellipse; the reason is that projection on the plane of the sky distorts shapes but preserves relative sizes of area elements because all are scaled by the common factor  $\cos i$ .

The line intensity of a non-rotating disk is  $I_v(R, i) = I_0(R, i)\Psi(v - v_0, R, i)$ , where  $I_0$  is the brightness at line center and  $\Psi$  is the spectral shape of the emerging line emission. When the line is optically thin,  $\Psi(v) = \Phi(v)$ . Determining  $\Psi$  for optically thick lines requires a full radiative transfer calculation; a sample of the results of such calculations is shown in fig. 1. In general,  $\Psi$  varies with  $i$  because of the variation of optical depth with inclination; it can also vary with  $R$  if the vertical optical depth varies with radius. Switching from frequency to equivalent velocity  $v = c(v_0 - \nu)/v_0$ , the profile becomes  $\Psi(v, i)$ , centered on  $v = 0$ . Now set the disk in Keplerian rotation  $v_{\text{rot}}(R)$ . For viewing angle  $i$ , the line-of-sight (los) component of the local rotation velocity of a point at radius  $R$  and angle  $\theta$  from the midline is

$$v_z(R, \theta, i) = v_{\text{out}} \left( \frac{R_{\text{out}}}{R} \right)^{1/2} \cos \theta, \quad \text{where } v_{\text{out}} = v_{\text{rot}}(R_{\text{out}}) \sin i \quad (7)$$

The line emission profile is now centered on  $v_z(R, \theta, i)$  and the monochromatic luminosity of a Keplerian disk is

$$L(v, i) = \int I_0(R, i) \Psi(v - v_z[R, \theta, i]) R dR d\theta \quad (8)$$

This is the basic expression for the spectral shape of disk line emission. In the case of a uniform disk the emerging profile involves simply the areal integration of the intrinsic emission profile  $\Psi$  with

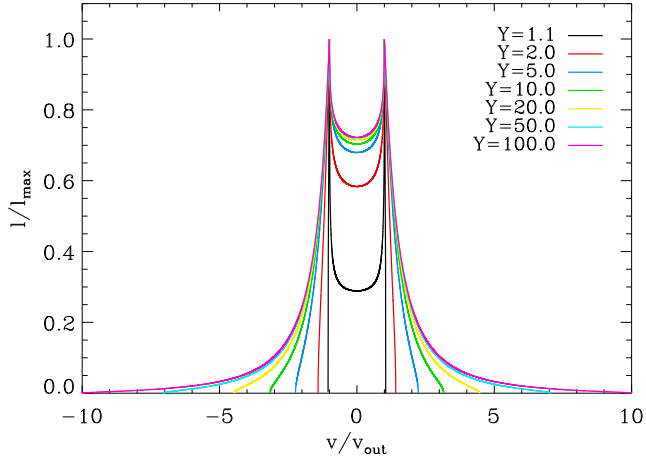


**Figure 5.** Lengths of iso-velocity contours for a Keplerian disk as a function of line-of-sight velocity for various values of the disk width  $Y = R_{\text{out}}/R_{\text{in}}$ .

the position variation introduced by the Keplerian rotation. We now present calculations for uniform disks ( $R$ -independent  $I_0$  and  $\Psi$ ) and various forms of  $\Psi$ . Although one can expect flaring and non-uniformity in physical disks, the uniform thin disk can be expected to faithfully reproduce the essence of the radiative transfer effects common to all disks.

### 3.2 Kinematic Double Peaks—Optically Thin Disks

The locus of all points whose emission is centered on the same frequency  $\nu$  is the constant los-velocity curve  $v_z = \nu$  on the surface of the disk. From eq. 7, for  $\nu \neq 0$  this curve obeys

$$R = R_{\text{out}} \left( \frac{v_{\text{out}}}{\nu} \right)^2 \cos^2 \theta \quad (9)$$

Figure 4 shows the contour plots of these curves for some representative velocities. In the case of a rectangular emission profile  $\Psi$ , the emission at  $\nu$  is proportional to the area of a strip centered on the corresponding contour. When the rectangular  $\Psi$  is so narrow that it can be approximated with a  $\delta$ -function, the emission becomes roughly proportional to the contour length. The shortest contour is the straight line at  $\nu = 0$ . With  $\nu$  increasing, as long as  $\nu < v_{\text{out}}$  the contours remain open, their curvature increases and with it their length. The first fully closed contour is the one for  $v_{\text{out}}$ , corresponding to the smallest los velocity on the disk midline. Increasing  $\nu$  further corresponds to smaller radial distances on the midline, and the contours are now shrinking, finally reaching the single point at the midline intersection with the inner radius where  $\nu = v_{\text{in}} (= v_{\text{out}} \sqrt{Y})$ . The contour lengths are calculated in closed form in Appendix B and plotted in figure 5 for various values of  $Y$  using the analytic result in eq. B2.

The variation of contour length with los velocity captures the essence of kinematic double-peaked profiles in Keplerian disks:  $v_{\text{out}}$  has the longest contour and thus produces peak emission. Figure 6 shows profiles calculated from eq. 8 with a Gaussian shape for the intrinsic line profile  $\Psi$  and increasing rotation velocity. The sequence is best understood by considering separately the emission from the approaching (left; fig. 4) and receding (right) halves of the rotating disk. With increasing rotation speed, the emission from each half is sliding outward in  $\nu$ , away from  $\nu = 0$ . As long as  $v_{\text{out}} \leq \Delta v_{\text{D}}$ , the emissions from both halves largely overlap and there are no double peaks. Increasing further the rotation velocity,

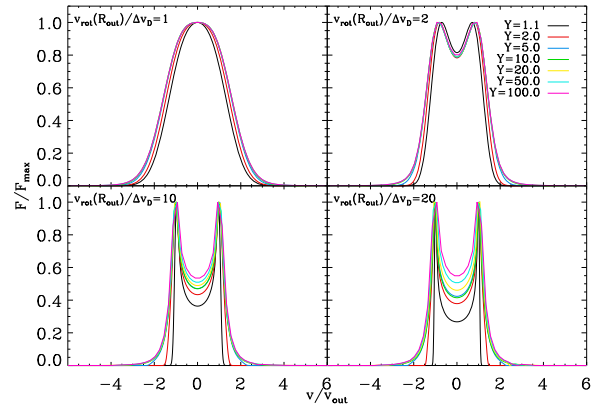


**Figure 6.** Spectral shape of the emission from Keplerian disks with Gaussian line profile  $\Psi_{\text{G}} = e^{-x^2}$  at increasing rotation velocity. The different curves in each panel cover a range of disk widths, as marked. These results should be applicable to optically thin disks (see eq. 11).

kinematic double peaks emerge, centered on  $\nu = \pm v_{\text{out}}$ , and the plots begin to resemble the behavior of the length contours (fig. 5). In particular, the profiles for  $v_{\text{out}} = 20\Delta v_{\text{D}}$  are quite similar to the length curves, and the depth ratio  $I_{\text{min}}/I_{\text{max}}$  for the central dip of a narrow disk (ring) with  $Y = 1.1$  is nearly the same as the corresponding length ratio. As the disk width increases, both the contour lengths and the emission profiles show quick transitions to limit ratios, albeit at different values. From analytic expressions developed in Appendix B we find that

$$\frac{I_{\text{min}}}{I_{\text{max}}} \simeq \begin{cases} \sqrt{Y-1} & Y < 2 \\ 4/3\pi & Y > 2 \end{cases} \quad (10)$$

Only narrow disks ( $R_{\text{out}} < 2R_{\text{in}}$ ) can produce kinematic double peaks with a central dip deeper than 0.4.

The Gaussian-profile results are applicable to optically thin lines and can be used to assess the disk parameters that will produce unequivocal kinematic double peaks. Since  $v_{\text{out}} = v_{\text{rot}}(R_{\text{out}}) \sin i$  (eq. 7), figure 6 shows that double peaks require not only  $v_{\text{rot}}(R_{\text{out}}) > \Delta v_{\text{D}}$  but also  $\sin i > \Delta v_{\text{D}}/v_{\text{rot}}(R_{\text{out}})$ . And since the los optical depth is  $\tau_{\text{T}}(i) = \tau_{\text{T}}/\cos i$ , the requirement of optically thin emission implies  $\cos i > \tau_{\text{T}}$ . Taken together, the parameter region

$$\tau_{\text{T}} < 1, \quad \frac{v_{\text{rot}}(R_{\text{out}})}{\Delta v_{\text{D}}} > 1, \quad \arcsin \frac{\Delta v_{\text{D}}}{v_{\text{rot}}(R_{\text{out}})} < i < \arccos \tau_{\text{T}} \quad (11)$$

will always produce kinematic double peak profiles.

### 3.3 Optically Thick Disks

Optical depth effects fall into two regimes according to the relation between the density and the transition critical density. When  $n \geq n_{\text{crit}}$  ( $\epsilon \geq 0.5$ ; eq. 1) the spatial variation of the source function is sufficiently small that the dip-to-peak contrast of the non-kinematic double peaks is diminished. Then the effect of increasing optical depth is mostly to flatten the top of the intrinsic emission profile and increase its width by a factor of  $\sim \sqrt{\ln \tau_{\text{T}}}$  (see §2). In this regime the profile  $\Psi_{\text{HM}} = 1 - e^{-\tau(x)}$  used in the Horne & Marsh (1986) calculations is a reasonable approximation for the exact solution of the line transfer problem. Figure 7 presents calculations with this profile, demonstrating the impact of line broadening with increasing optical thickness of the Keplerian disk. Because of the

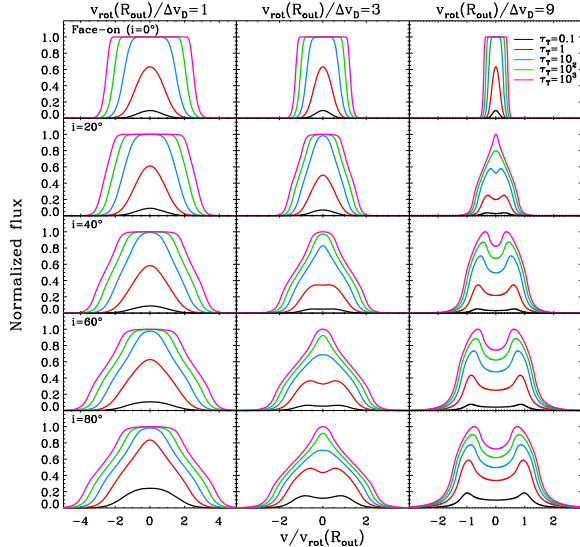


**Figure 7.** Spectral shape of the emission from Keplerian disks with the Horne & Marsh profile  $\Psi_{\text{HM}} = 1 - e^{-\tau(x)}$ . These results should be applicable to sources with  $n \geq n_{\text{crit}}$  ( $\epsilon \geq 0.5$ ; see §3.3). The disk radial thickness is  $R_{\text{out}}/R_{\text{in}} = 10$ , the rotation velocity ranges from  $v_{\text{rot}}(R_{\text{out}})$  on the outer edge to  $v_{\text{rot}}(R_{\text{in}}) = \sqrt{10} v_{\text{rot}}(R_{\text{out}})$  on the inner one. Rows correspond to various inclinations, as marked, columns show a progression of rotation velocities; the apparent profile narrowing between columns arises from the scale change of the velocity axis. In each panel, line colors correspond to different values of  $\tau_T$ , the vertical optical depth, as marked, and the emission is normalized to a maximum of unity.

dependence of los optical depth on  $i$ , the viewing angle now affects not only the los velocity but also the intrinsic profile shape. Whereas the viewing angle effect was fully absorbed into  $v_{\text{out}}$  in the two previous figures, now it must be shown explicitly. The columns in figure 7 show the effect of increasing rotation velocity while the rows show the effect of increasing viewing angle. The top row shows disks viewed face-on, demonstrating the profile broadening with vertical optical depth<sup>1</sup>. In addition to its impact on the profile shape, the optical depth affects also the intensity scale—emission from optically thin disks is reduced by a factor of  $\tau_T/\cos i$  from that of optically thick disks with the same source function.

When  $n < n_{\text{crit}}$  ( $\epsilon < 0.5$ ), optical depth effects introduce non-kinematic double peaks in addition to broadening the emission spectral range (§2). This region requires full solution of the radiative transfer problem, and we utilize the emission profiles  $\Psi(x)$  from the slab solution (see fig. 1) in the fundamental relation for emission from rotating disks (eq. 8). Figure 8 shows the results for uniform disks with  $\epsilon = 10^{-2}$  and various optical depths, rotating at increasing velocities and viewed from different directions; these results are representative of the  $\epsilon < 0.5$  domain. As in figure 7, the intensity is lower in the optically thin region because of the smaller emitting column. Additionally, the intensity at low optical depths is now further reduced because of the decrease in line excitation temperature, reflecting the sub-thermal level populations. The face-on disks shown in the top row replicate the behavior seen in fig. 1: Gaussian profiles when  $\tau_T \leq 1$ , non-kinematic double peaks for the optically thick disks.

<sup>1</sup> The row’s three panels are identical; the apparent narrowing with rotation velocity simply reflects the scaling of the  $x$ -axis with  $v_{\text{rot}}(R_{\text{out}})$ .

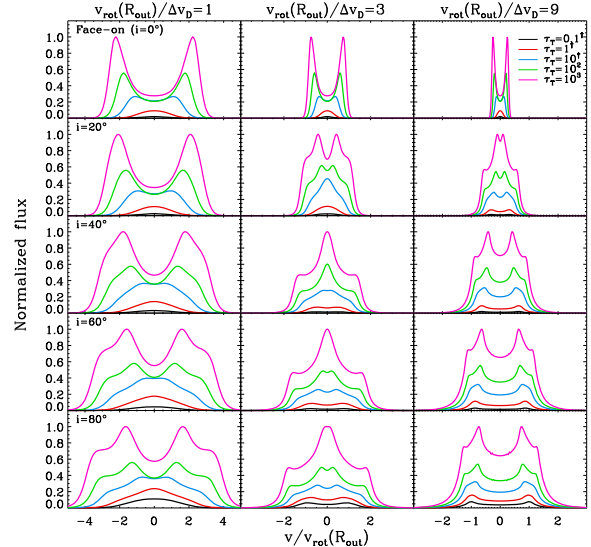


**Figure 8.** Frequency profiles, normalized to unity peak in each panel, of line emission from uniform, flat Keplerian disks. The intrinsic emission profile  $\Psi(x)$  is obtained from the radiative transfer solution for a slab with photon destruction probability  $\epsilon = 10^{-2}$  and optical depth as marked. All other disk properties are the same as in figure 7. For clarity, the results for  $\tau_T = 0.1, 1$  and  $10$ , marked by †, were multiplied by  $15, 5$  and  $2$ , respectively.

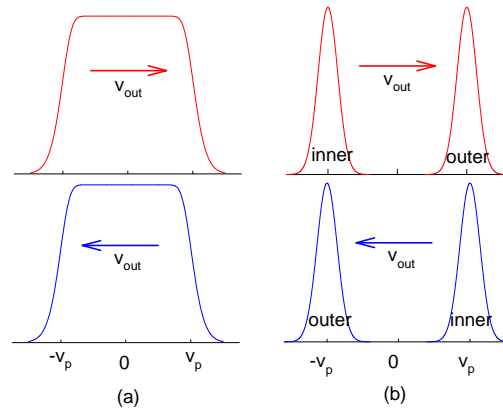


**Figure 9.** Disk rotation and optically thick line emission. Shown are schematic illustrations of the stationary-disk profiles when (a)  $n > n_{\text{crit}}$  and (b)  $n < n_{\text{crit}}$ . In both cases, rotation shifts to the right (left) the emission from the receding (approaching) half of the disk by the amount  $v_{\text{out}}$ . In (b), the leading non-kinematic peaks are labeled “outer”, the trailing ones “inner”. The outer peaks are always moving away from each other, the inner ones are first approaching and then receding as  $v_{\text{out}}$  increases.

The effects of rotation on observed profiles at slanted viewing are broadly similar in both figures 7 and 8 and can be readily understood with the aid of the illustrations in figure 9 that sketch schematically the disk intrinsic profile in each case. Introduce  $v_p = \Delta v_D \sqrt{\ln(\tau_T/\cos i)}$ . Then the  $n > n_{\text{crit}}$  profile can be described with a flat top for  $|v| < v_p$  (figure 9a) while the intrinsic  $n < n_{\text{crit}}$  profile can be taken as just two peaks with centers at  $v = \pm v_p$  and width  $\sim \Delta v_D$  (fig. 9b). The top and bottom of each panel illustrate the emission from each half of a stationary disk. When the disk is set in rotation, the profiles of the two halves slide against each other in opposite directions away from the center  $v = 0$ ; the emission from the approaching half (blue profile) is shifted

by  $v_{\text{out}}$  (eq. 7) to the left, from the receding half (red) to the right by the same amount. Full kinematic separation of the emission from the two halves of the disk occurs only when  $v_{\text{out}} > v_p + \Delta v_D$  and the trailing edge of each profile crosses the center. Thus the criterion for emergence of kinematic double structures is now

$$\frac{v_{\text{rot}}(R_{\text{out}})}{\Delta v_D} \sin i > \sqrt{\ln(\tau_T / \cos i)} + 1 \quad (12)$$

This replaces eq. 11 as the condition for kinematic double peaks when the disk is optically thick rather than thin. At any given  $\tau_T$  ( $> 1$ ), this condition can be met only for sufficiently large viewing angles and rotation speeds. For  $\tau_T > 10$  this criterion is met in the right column panels of figures 7 and 8, where  $v_{\text{rot}}(R_{\text{out}}) = 9\Delta v_D$ . At lower rotation velocities the blue and red profiles partially overlap, resulting in the central peak evident in the mid-columns of figures 7 and 8 in the  $i \geq 40^\circ$  panels. The central peak is produced for rotation velocities in the range  $v_p - \Delta v_D < v_{\text{out}} < v_p + \Delta v_D$ , namely

$$\sqrt{\ln(\tau_T / \cos i)} - 1 < \frac{v_{\text{rot}}(R_{\text{out}})}{\Delta v_D} \sin i < \sqrt{\ln(\tau_T / \cos i)} + 1 \quad (13)$$

and it covers the spectral overlap region  $|v| < v_{\text{out}} - v_p + \Delta v_D$ .

Because of its greater intrinsic complexity, the non-kinematic double-peaked profile of  $\epsilon < 0.5$  sources produces some additional structure in rotating disks. In the schematic sketch of figure 9, the leading peak of the emission from each half of the disk is labeled “outer”, the trailing one “inner”. Rotation shifts the outer peaks away from the center and their separation increases monotonically with the rotation speed. These peaks are discernible in the  $i > 20^\circ$  panels of figure 8 as the outermost bumps at  $v = \pm(v_{\text{out}} + v_p)$  in the profiles for all  $\tau_T \geq 10$ ; they are always the lowest structures, reflecting emission from only half of the disk. The inner peaks first approach each other, then overlap to produce the central peak (eq. 13) and finally move away from each other once their trailing edges cross the center (eq. 12). This final regime produces the quadruple-peak profiles evident in the right-column panels for  $\tau_T > 10$  and  $i \geq 20^\circ$ . Here the intrinsic non-kinematic double-peaked profiles are superposed on the underlying kinematic double-peaks with their centers shifted to  $\pm v_{\text{out}}$ . The kinematic separation produced by rotation is centered on the dip between each pair of non-kinematic peaks, and not on the prominent inner peaks; the markers of the rotation velocity are these dips. Quad-peak profiles are seen also in the left column of figure 8 in the  $i \geq 60^\circ$  panels for  $\tau_T \geq 100$ . These quad-peaks occur at low velocities,  $v_{\text{out}} < v_p - \Delta v_D$ , when the leading edge of each inner peak has not yet reached the center. The two doublets making up the quad are centered on  $\pm v_p$ , comprised each of the outer peak of emission from one half of the disk and the inner peak from the other half. The separation between the peaks of the two members of each doublet is  $2v_{\text{out}}$  and the separation between their prominent, inner peaks is  $2(v_p - v_{\text{out}})$ . The inner pair of peaks is higher than the outer one because they get contributions from the two underlying non-kinematic peaks.

#### 4 DISCUSSION

Double-peaked line profiles can arise from kinematic motions such as disk rotation, collapse or bipolar outflow. In particular, rotating disks produce such profile shapes for rotation velocities that obey the relations in eq. 11 when  $\tau_T < 1$  or eq. 12 when  $\tau_T > 1$ . However, double-peaked profiles arise also in the emission from stationary optically thick sources when the density is below the critical density. There is no obvious way to choose between these two possibilities from the profile shape alone since non-kinematic double

peak profiles of face-on disks with  $\tau_T \geq 10$  (fig. 8) are quite similar to their kinematic counterparts in optically thin slanted disks (fig. 6). Because there is no clear-cut distinction between the two cases, a double-peaked shape must be supplemented by additional information before it can be taken as the signature of a rotating disk. Such independent input generally involves the line optical depth. When a transition is known to be optically thin in a given source, double-peaked emission can be reliably attributed to kinematic effects and eq. 11 then constrains the source parameters. The depth of the central dip is limited in that case to  $I_{\text{min}}/I_{\text{max}} \gtrsim 0.4$  in all but narrow disks (eq. 10). A deeper central dip implies a narrow, ring-like emission region with  $R_{\text{out}} < 2R_{\text{in}}$ .

When the possibility exists that a line is optically thick the situation is more involved because double-peaked profiles can then arise from either rotation or radiative transfer or both. If it is known additionally that  $n \geq n_{\text{crit}}$  then double-peaks convincingly imply a kinematic origin because the intrinsic profile is nearly flat top (fig. 7). However, when there is reason to believe that  $n$  could be less than  $n_{\text{crit}}$  then disk rotation can be deduced only if it can be shown that the peak separation exceeds  $\Delta v_D \sqrt{\ln(\tau_T / \cos i)}$  for all reasonable estimates of  $\Delta v_D$  and  $\tau_T$ . While this is not always possible, the triple and quadruple profiles seen in figure 8 can be used instead to identify optically thick rotating disks. Indeed, in certain circumstances these complex profile shapes could be more reliable indicators of rotation because they cannot be produced by radiative transfer alone. The emergence of these profiles is a robust result (see §3.3, especially fig. 9) that should not depend on the simplifying assumptions in our numerical calculations.

To demonstrate the formation of double-peaked profiles in the absence of any large scale motions we presented here the simplest line transfer problems with the minimal number of free parameters. In particular, we considered a single two-level transition with line excitation purely by collisions in an environment with constant temperature and density. However, the results remain applicable for a much larger set of conditions because the central dip arises from the decrease of the line excitation temperature away from the center toward the surface of the source. This decrease arises purely from radiative transfer effects in our simplified models, but it is expected in most environments with variable physical conditions because temperature and density generally decrease outward, amplifying the effect. A line excitation temperature that instead increases toward the surface is possible only under rather special circumstances, such as temperature inversion for example, and our results would not be applicable in such cases. Similarly, our calculations employed only the Gaussian line profile (implicitly assuming complete redistribution) but the emergence of the central dip depends on the fact that the line profile decreases toward the wings, not on the specific shape of this decrease. The dip occurs because the emission at the line core follows the spectral variation of  $S[1/\Phi(x)]$  (see §2 and eq. A3), thus the Lorentzian profile would produce the dip just the same, albeit with a somewhat different shape. Finally, the disk analysis presented here was performed for simplicity in the thin disk approximation. Taking account of the vertical variation of physical parameters requires a more elaborate calculation that adds more free parameters (e.g. Asensio Ramos et al. 2007) but is not expected to affect significantly the profile shapes found here. Our results should remain valid as long as the viewing angle is such that the disk edge contribution remains negligible and the absorption of the continuum does not play an important role (as, for example, in the case of water lines: Cernicharo et al. 2009; Ceccarelli et al. 2010). The calculations were conducted for uniform disks, with  $R$ -independent line-center intensity  $I_0(R)$ . They are applicable to other

situations because a disk whose  $I_0(R)$  declines steeply with  $R$  can be approximated with a uniform disk whose boundaries are limited to the peak emission region. This explains the Horne & Marsh (1986) modeling results for the eclipsing dwarf nova Z Cha. The double peaked profile in this source has  $I_{\min}/I_{\max} = 0.4$ , roughly the deepest dip possible for optically thin Keplerian disks with  $R_{\text{out}} \geq 2R_{\text{in}}$ . While the Horne & Marsh model disk had a much larger  $R_{\text{out}} \sim 10R_{\text{in}}$ , it also had  $I_0(R) \propto 1/R^2$ . This steep intensity decline ensures an effectively ring-like emission region that enabled reproduction of the observed contrast.

Our results show that detection claims of disks based on double-peaked profiles of molecular lines must be always scrutinized carefully for optical depth effects. Double-peaked profiles of presumably optically thin lines (e.g. from rare isotopes) can be used reliably for identifying candidate disks around YSO whose average sizes are too small to be resolved even with ALMA. The case of AGN, where double peaked H $\alpha$  and Mg II  $\lambda 2798$  profiles were interpreted as rotating disk emission (Eracleous et al. 2009), is more complicated. Because their excitations are driven by photoionization and not collisions, our model calculations are not directly applicable to these lines. Still, their large optical depths,  $\sim 10^5$ – $10^6$  (H. Netzer, private communication), imply that the source function is unlikely to be constant in either case, triggering the non-kinematic double peaked shapes seen in §2. An actual estimate of this effect will require detailed photoionization model calculations coupled with exact radiative transfer calculations for these lines instead of the common escape probability approach.

## APPENDIX A: SLAB ANALYTIC APPROXIMATIONS

Neglecting radial coupling, the radiative transfer problem of a face-on flat disk is identical to that of a slab, as noted above (§3). Here we present some approximate analytic expressions that reproduce adequately the solution of the slab problem.

The two-level problem in a flat uniform slab is fully defined by the photon destruction probability  $\epsilon$  and the total optical depth  $\tau_T$  across the slab. Positions in the slab are characterized by the vertical distance  $\tau$  from one face,  $0 \leq \tau \leq \tau_T$ . The formal solution for the intensity emerging perpendicular to the slab face is

$$I(x) = \Phi(x) \int_0^{\tau_T} S(\tau) e^{-(\tau_T - \tau)\Phi(x)} d\tau \quad (\text{A1})$$

Whenever  $\tau_T \Phi(x) < 1$ ,

$$I(x) \simeq \Phi(x) \int_0^{\tau_T} S(\tau) d\tau = \bar{S} \tau_T \Phi(x) \quad (\text{A2})$$

where  $\bar{S}$  is the value of the source function at some (a-priori unknown) point inside the slab. We approximate the emission in the optically thin wings ( $\tau_T \Phi(x) < 1$ ,  $|x| > x_w$ ; see eq. 3) with this expression. In the optically thick core ( $\tau_T \Phi(x) > 2$ ,  $|x| < x_c$ ), according to the Eddington-Barbier relation the radiation emerges from an optical depth of  $\sim 1$  from either surface, therefore the intensity is approximately  $S[\tau = 1/\Phi(x)]$ . The frequency range  $x_c \leq |x| \leq x_w$ , where  $2 \geq \tau_T \Phi(x) \geq 1$ , does not lend itself naturally to any physical approximation since the optical path is thick to one surface and thin to the other (except for the midplane where both paths are optically thin). However, this is a small spectral region whose relative thickness  $(x_w - x_c)/x_c$  decreases with overall optical depth (eq. 3), therefore we approximate the intensity there with a constant. Joining smoothly the core and wing approximations with this constant yields  $\bar{S} = S(\tau_T/2)$  — the unknown  $\bar{S}$  is the source function on the

slab midplane. Thus our approximation for the emergent radiation is

$$I(x) \simeq \begin{cases} S[1/\Phi(x)] & |x| < x_c \\ S(\tau_T/2) & x_c \leq |x| \leq x_w \\ S(\tau_T/2) \tau_T \Phi(x) & |x| > x_w \end{cases} \quad (\text{A3})$$

Completion of the intensity expression requires an approximation for the  $\tau$ -variation of  $S$  inside the slab. Motivated by Eq. 2.18 of Avrett & Hummer (1965), we fitted the source function throughout the slab with the following empirical expression containing the free parameters  $a$ ,  $b$  and  $\alpha$ :

$$S(\tau; \epsilon, \tau_T) = a + b k_1(\epsilon^\alpha \tau), \quad (\text{A4})$$

where

$$k_1(\tau) = 1 - \frac{1}{2} [K_2(\tau) + K_2(\tau_T - \tau)]$$

and

$$K_2(\tau) = \frac{1}{\sqrt{\pi}} \int_{-\infty}^{\infty} \Phi(x) E_2[\tau \Phi(x)] dx,$$

with  $E_2$  the 2nd exponential integral. We find that  $\alpha = 0.7$  yields satisfactory agreement with the exact numerical solutions for all values of  $\epsilon$  and  $\tau_T$ . The constants  $a$  and  $b$  are related to the values of the source function on the slab surfaces and its midplane via

$$\begin{aligned} a &= S(0) - b k_1(0) \\ b &= \frac{S(\tau_T/2) - S(0)}{k_1(\epsilon^\alpha \tau_T/2) - k_1(0)} \end{aligned} \quad (\text{A5})$$

The values of  $S(0)$  and  $S(\tau_T/2)$  can be approximated utilizing some general properties of the slab radiative transfer problem derived in Avrett & Hummer (1965). They show that the source function on the surface of a slab with an overall optical depth  $\tau_T$  can be related to that at depth  $\tau_T$  into a semi-infinite atmosphere. For the latter problem there exist some general theorems in the limits of both large and small  $\epsilon$ . Utilizing those, we devised the following simple relations:

$$\begin{aligned} S(\tau_T/2) &= \frac{\epsilon + \epsilon \tau_T}{1 + \epsilon \tau_T} B \\ S(0) &= \sqrt{\epsilon} \frac{\sqrt{\epsilon} + \beta_1 (\epsilon \tau_T)^{p_1} + \beta_2 (\epsilon \tau_T)^{p_2}}{1 + \beta_1 (\epsilon \tau_T)^{p_1} + \beta_2 (\epsilon \tau_T)^{p_2}} B, \end{aligned} \quad (\text{A6})$$

where  $B$  is the Planck function of the (constant) slab temperature. We find that  $S(0)$  is reproduced satisfactorily with  $\beta_1 = 1.41$ ,  $\beta_2 = 1.23$ ,  $p_1 = 0.6$  and  $p_2 = 0.55$ . This completes our analytic approximation for  $S(\tau)$  in all slabs. Inserting this expression in the approximation for the emerging intensity (eq. A3) produces the line profiles shown in figure A1. These profiles are calculated for the same parameters used in the exact model calculations presented in figure 1. Comparison of the two verifies the adequacy of the analytic approximation provided by the combination of equations A3 through A6.

The depth of the central dip in double-peaked profiles can be characterized by the ratio of intensities at line center and at the peaks. From eq. A3,

$$\frac{I_{\min}}{I_{\max}} = \frac{I(x=0)}{I(x=x_c)} \simeq \frac{S(\tau=1)}{S(\tau=\tau_T/2)} \quad (\text{A7})$$

This expression provides an excellent approximation for the exact results shown in figure 3 for the variation of the central dip with optical depth for various values of  $\epsilon$ , but  $S(\tau=1)$  is not easily discernible from the somewhat involved approximation for the source function. Neglecting the variation of  $S$  close to the slab surface and

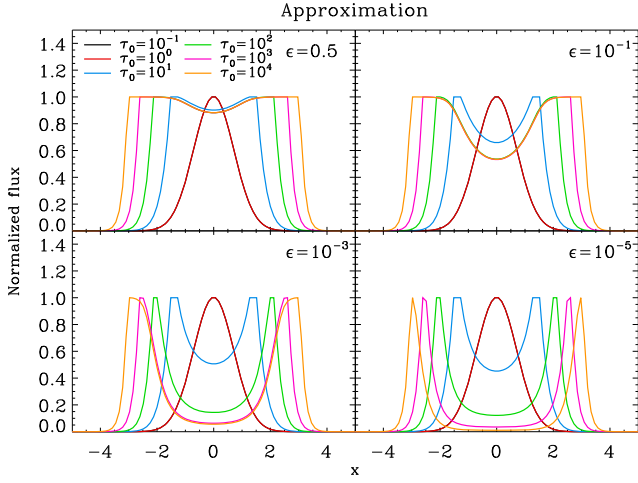


**Figure A1.** Line radiation emergent from slabs with the parameters of the models displayed in figure 1. These profiles were calculated analytically by combining the approximate expressions in equations A3 through A6.

replacing  $S(1)$  with  $S(0)$ , which is given explicitly in eq. A6, yields the simpler, though somewhat less accurate, result

$$\frac{I(x=0)}{I(x=x_c)} \approx \frac{S(\tau=0)}{S(\tau=\tau_T/2)} \quad (\text{A8})$$

Combining this relation with eq. A6 produces the approximation given in eq. 4.

## APPENDIX B: KEPLERIAN CONTOURS

All points on the disk surface whose emission is centered on the same frequency  $\nu$  lie on the contour defined in eq. 9. The polar angle varies on the contour between the inner and outer radii in the range  $[\theta_{\text{in}}, \theta_{\text{out}}]$ , where

$$\theta_{\text{in}} = \arccos \frac{\nu}{v_{\text{in}}}, \quad \theta_{\text{out}} = \begin{cases} \arccos \frac{\nu}{v_{\text{out}}} & 0 \leq \nu \leq v_{\text{out}} \\ 0 & v_{\text{out}} \leq \nu \leq v_{\text{in}} \end{cases} \quad (\text{B1})$$

Straightforward integration produces the contour length

$$\ell(\nu) = R_{\text{out}} \left( \frac{v_{\text{out}}}{\nu} \right)^2 [f(\theta_{\text{in}}) - f(\theta_{\text{out}})] \quad (\text{B2})$$

where

$$f(\theta) = \sin \theta \sqrt{1 + 3 \sin^2 \theta} + \frac{1}{\sqrt{3}} \ln \left( \sqrt{3} \sin \theta + \sqrt{1 + 3 \sin^2 \theta} \right)$$

This relation produces the profiles shown in figure 5. Comparison with fig. 6 shows good agreement with the results of full calculations with narrow-width Gaussian shape for the intrinsic line emission. In particular, the depth  $I_{\text{min}}/I_{\text{max}}$  of the central dip is nearly the same for the narrow disk (ring) with  $Y = 1.1$  as the length ratio  $\ell_{\text{min}}/\ell_{\text{max}}$  for the same  $Y$ . Therefore, we can use the contour length for an estimate of the central dip depth contrast in narrow disks:

$$\frac{I_{\text{min}}}{I_{\text{max}}} \underset{Y \gg 1}{\approx} \frac{\ell_{\text{min}}}{\ell_{\text{max}}} \quad (\text{B3})$$

The longest contour,  $\nu = v_{\text{out}}$ , has  $\theta_{\text{out}} = 0$  and  $\theta_{\text{in}} = \arccos Y^{-1/2}$  so that

$$\ell_{\text{max}} = R_{\text{out}} f \left( \sqrt{\arccos Y^{-1/2}} \right) \underset{Y \gg 1}{\rightarrow} 2R_{\text{out}} \sqrt{Y-1} \quad (\text{B4})$$

while the length of the shortest contour,  $\nu = 0$ , is simply

$$\ell_{\text{min}} = 2R_{\text{out}}(Y-1). \quad (\text{B5})$$

Combining the last three relations produces the narrow-disk result listed in eq. 10.

Although the length calculation reproduces reasonably well the profile shape and  $Y$ -dependence also for wide disks ( $Y \gg 1$ ; see figures 5 and 6), it misses on the actual value of  $I_{\text{max}}/I_{\text{min}}$ , the dip contrast; the length calculation produces accurately the central contrast for narrow disks but not for the thicker ones because of a fundamental issue with the approach to a  $\delta$ -function limit. The line profile can be considered narrow when  $\Delta v_{\text{D}} \ll v$ , and this condition is never applicable at line center, where  $v = 0$ . Since the line wings of the closed contours contribute more to the  $v > 0$  contours of wide disks, the length calculation misses the proper result; instead, a calculation of the emitting area at velocity  $\nu$  is necessary. The area under the  $\nu$ -contour in the 1st quadrant is

$$A(\nu) = \frac{1}{2} R_{\text{out}}^2 \left( \frac{v_{\text{out}}}{\nu} \right)^4 [g(\theta_{\text{in}}) - g(\theta_{\text{out}})] \quad (\text{B6})$$

where

$$g(\theta) = \frac{3}{8} \theta + \frac{3}{8} \sin \theta \cos \theta + \frac{1}{4} \sin \theta \cos^4 \theta$$

At large  $Y$  we have  $\theta_{\text{in}} \simeq \pi/2$  for the  $v_{\text{out}}$ -contour (eq. B1) so that  $g(\theta_{\text{in}}) = \frac{3}{16} \pi$  and the area under contours close to the longest one is

$$\nu \simeq v_{\text{out}} : \quad A(\nu) \simeq \frac{3\pi}{32} R_{\text{out}}^2 \left( \frac{v_{\text{out}}}{\nu} \right)^4 \quad (\text{B7})$$

For a rectangular velocity profile with width  $\Delta v_{\text{D}} \ll v_{\text{out}}$ , it is straightforward to show from this expression that the area of peak emission in the 1st quadrant is

$$A_{\text{peak}} = A(v_{\text{out}} - \Delta v_{\text{D}}) - A(v_{\text{out}}) = \frac{3\pi}{8} R_{\text{out}}^2 \frac{\Delta v_{\text{D}}}{v_{\text{out}}} \quad (\text{B8})$$

At line center ( $\nu = 0$ ) the emitting area in the first quadrant is between the vertical axis and a roughly radial ray with  $\nu = \Delta v_{\text{D}}$ . This ray has inclination  $\Delta v_{\text{D}}/v_{\text{out}}$  to the  $y$ -axis so that the area of dip emission is

$$A_{\text{dip}} = \frac{1}{2} R_{\text{out}}^2 \frac{\Delta v_{\text{D}}}{v_{\text{out}}} \quad (\text{B9})$$

Therefore, the limiting depth is

$$\frac{I_{\text{min}}}{I_{\text{max}}} = \frac{A_{\text{dip}}}{A_{\text{peak}}} \underset{Y \gg 1}{\approx} \frac{4}{3\pi} \quad (\text{B10})$$

This result, listed in eq. 10, reproduces fairly accurately the depth contrast of the narrowest Gaussian profile ( $\Delta v_{\text{D}}/v_{\text{out}} = 1/20$ ) in figure 6.

## REFERENCES

- Asensio Ramos A., Ceccarelli C., Elitzur M., 2007, *A&A*, 471, 187  
 Avrett E. H., Hummer D. G., 1965, *MNRAS*, 130, 295  
 Ceccarelli C., Cernicharo J., Ménard F., Pinte C., 2010, *ApJ*, 725, L135  
 Cernicharo J., Ceccarelli C., Ménard F., Pinte C., Fuente A., 2009, *ApJ*, 703, L123  
 Elitzur M., 1992, *Astronomical Masers*. Kluwer Academic Publishers  
 Elitzur M., Asensio Ramos A., 2006, *MNRAS*, 365, 779  
 Eracleous M., Lewis K. T., Flohic H. M. L. G., 2009, *New Astronomy Review*, 53, 133



- Greenhill L. J., 2007, in IAU Symp 242: Astrophysical Masers and their Environments Masers in AGN environments. pp 381–390
- Horne K., Marsh T. R., 1986, MNRAS, 218, 761
- Hummel W., 2000, in Smith M. A., Henrichs H. F., Fabregat J., eds, IAU Colloq. 175: The Be Phenomenon in Early-Type Stars Vol. 214 of ASP Conf. Ser., Line Profile Modeling of Disks. p. 396
- Pavlyuchenkov Y., Semenov D., Henning T., Guilloteau S., Piétu V., Launhardt R., Dutrey A., 2007, ApJ, 669, 1262
- Zhang X.-G., Dultzin D., Wang T.-G., 2008, in RMxAC vol 32 How to accurately estimate BH masses of AGN with double-peaked emission lines. pp 43–45